JACS
JOURNAL OF THE AMERICAN CHEMICAL SOCIETY

pubs.acs.org/JACS
Article

Metal–Metal Oxide Interaction Modulated Photocatalytic Methane Conversion

Yanzhao Zhang, Jiakang You, Kai Wang, Dazhi Yao, Haijiao Lu, Jitraporn Vongsvivut, Jingwei Hou, Peng Chen, Yonggang Jin, Gang Liu, Zhiliang Wang,* and Lianzhou Wang*

Cite This: *J. Am. Chem. Soc.* 2026, 148, 17094–17103

Read Online

ACCESS | Metrics & More | Article Recommendations | Supporting Information

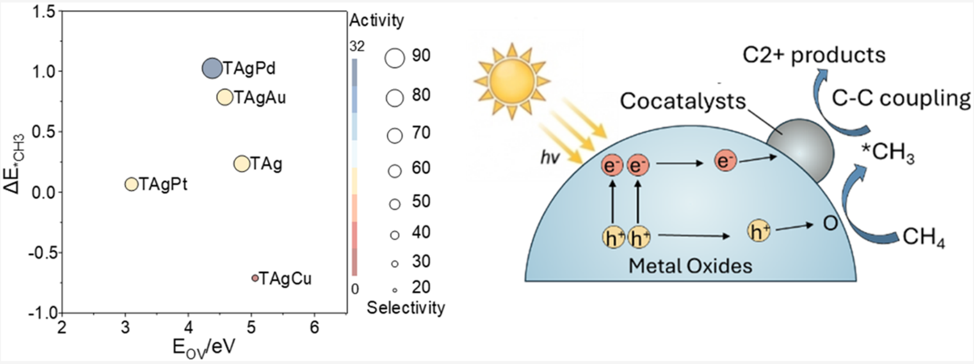

ABSTRACT: Metal–metal oxide (M–MO) interactions are important in catalysis. However, insights into how such interactions modulate lattice oxygen activity and stabilize critical reaction intermediates are scarce. In this work, using photocatalytic oxidative coupling of methane (POCM) as an example, we develop a simple and predictive model that defines M–MO interactions using two key factors: oxygen vacancy formation energy (E_{OV}) and the methyl (*CH$_3$) adsorption energy difference (ΔE_{*CH_3}) across metal and oxide sites. Interfacial coupling comodulates E_{OV} and ΔE_{*CH_3}. E_{OV} governs lattice-oxygen reactivity and the initial C–H activation, while ΔE_{*CH_3} controls CH$_3$ distribution between metal and oxide sites and thereby C–C coupling selectivity. Correlating E_{OV} and ΔE_{*CH_3} with activity and selectivity reveals a unifying principle. Efficient methane conversion requires moderately labile lattice oxygen whereas selective C–C bond formation demands a large ΔE_{*CH_3} to drive methyl coupling for multicarbon products. Specifically, a AgPd/TiO$_2$ catalyst achieves an optimal balance in experimental testing, delivering over a methane conversion yield of 30 mmol g^{-1} h^{-1}, a selectivity of 92% for C$_2$ products, and an operation stability of around 160 h. More broadly, the E_{OV}–ΔE_{*CH_3} framework provides a predictive descriptor map for M–MO photocatalysts selection in POCM. This study fills a critical gap by establishing a quantitative framework for M–MO interactions, identifying interfacial synergy as the principal determinant of performance, and enabling rational M–MO catalyst design.

INTRODUCTION

Metal–metal oxide (M–MO) interactions represent a fundamental design principle in functional materials, as interfacial charge transfer and electronic modulation at these junctions create properties that govern overall performance across diverse applications. Supported metals, exemplify this concept and are widely applied in heterogeneous catalysis,[1−4] energy storage,[5] gas sensing,[6] and electronic devices.[7] Their activity often arises from the unique synergy at the M–MO interface, where interactions are inherently bidirectional.[8−10] On one hand, MO supports can modulate the electronic structure, dispersion, and stability of the metal component.[11,12] On the other hand, deposited metals can profoundly change the MO substrate by inducing oxygen vacancies, modifying the band structure, and reshaping surface chemistry.[2,13,14] The significance of M–MO interactions has received intensive attention in conventional catalysis, but remains insufficiently explored in the emerging photocatalysis process. Taking photocatalytic oxidative coupling of methane (POCM) as an example, a range of metallic catalysts, including single atoms,[10,15,16] nanoparticles,[6,13] nanoalloys,[2,9] and compounds,[17,18] have been employed to enhance photocatalytic

Received: January 25, 2026
Revised: April 6, 2026
Accepted: April 9, 2026
Published: April 16, 2026

https://doi.org/10.1021/jacs.6c01783
J. Am. Chem. Soc. 2026, 148, 17094–17103

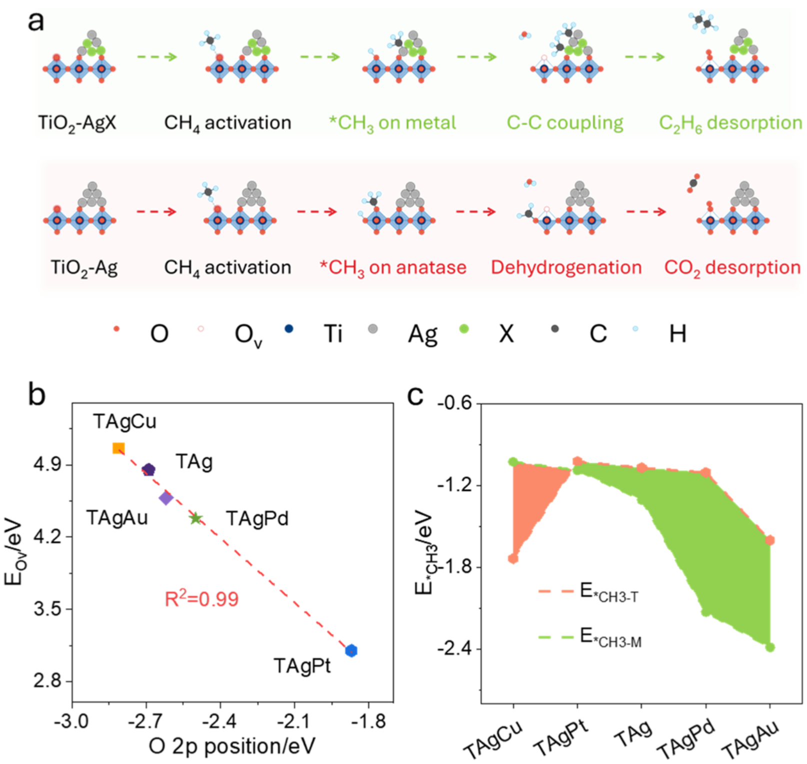

Figure 1. Proposed reaction mechanism and theoretical prediction of activity−selectivity relationships in POCM. (a) Schematic illustration of M−MO interaction between supported metal cocatalysts and the TiO_2 lattice oxygen mechanism for POCM toward different products; (b) correlation between E_{OV} and the O 2p band onset, suggesting that O 2p band alignment governs oxygen vacancy formation; (c) adsorption energies of $*CH_3$ on anatase TiO_2 and different supported metals, where stronger $*CH_3$ stabilization on AgPd is linked to enhanced surface coupling. The red and green areas indicate regions where methyl species exhibit stronger adsorption on anatase TiO_2 and the supported metal sites, respectively.

performance. However, fundamental questions remain unclear on how M−MO interactions regulate the generation, stabilization, and conversion of key intermediates, which ultimately determine the activity and selectivity of POCM.

In POCM, lattice oxygen of MO is regarded as the active species for the initial cleavage of the C−H bond for the generation of key intermediates of methyl radicals ($*CH_3$).[9,19] The subsequent behavior of $*CH_3$ is strongly influenced by the M−MO interaction. When $*CH_3$ migrates to metal sites, C−C coupling can be promoted with the formation of C_2 hydrocarbons such as ethane and ethylene (C_2 generation pathway).[9,20−22] If, however, $*CH_3$ remains confined to the MO surface, it undergoes deep oxidation, producing CO_2 as the major products (CO_2 generation pathway). The reaction pathways are governed by the composition of metal and the MO substrate, as well as by the interactions between them. Previous research indicates that despite the same photocatalyst (e.g., TiO_2), the methane conversion and product selectivity show a remarkable dependence on metal cocatalysts such as Au,[6,23] Ag,[24] Pt,[2,13] and Pd.[25] It is speculated that metal can dramatically influence metal oxides and regulate the reactivity of lattice oxygen. In turn, metal oxide can modulate the electronic structure of the metal cocatalyst, leading to tunable adsorption strength of surface intermediates. This has been reflected in product selectivity dependence on various metal oxides with Au as the cocatalysts.[10,21] Despite the trial-and-error efforts, there is very limited understanding about the intrinsic features of M−MO interaction in a M−MO photocatalysts in determining the activity and selectivity in POCM.

On the other hand, the effects of cocatalysts can be strongly modulated by their composition and structure. For example, an AgAuCu alloy enhances ethylene production compared with monometallic Cu,[26] because the incorporation of Ag and Au suppresses the formation of intermediates such as $*C_2H_5$ and $*C_2H_2$, thereby improving ethylene selectivity. Furthermore, the introduction of heterometallic sites induces electronic perturbations and reshapes the local chemical environment, which can facilitate the C−C coupling.[27] The presence of multiple metal sites significantly modifies the adsorption energies of key intermediates, and therefore steers the reaction pathway. For instance, AuPd nanoalloys can stabilize $*CH_2$ intermediates and thereby strongly promote ethylene formation.[28]

In this work, we move beyond the qualitative view of M−MO interaction as "strong or weak" and parametrize it with two transferable descriptors: oxygen vacancy formation energy (E_{OV}) in MO and $*CH_3$ adsorption energy difference (ΔE_{*CH_3}) at the M−MO interface. Considering the high performance and modulational flexibility of sliver in reported references,[23,24] density functional theory (DFT) calculations across a series of Ag-based metals supported on TiO_2 shows a significant change of E_{OV} and ΔE_{*CH_3} depending on the bimetal compositions (Ag incorporated with Pd, Pt, Cu, and Au, denoted as TAgX, T represent TiO_2, X indicates the same atomic amount of second metal composition). Further experimental evaluation on the POCM performance of the corresponding photocatalysts revealed strong relationships of activity E_{OV} and selectivity ΔE_{*CH_3}, respectively. Specifically, small E_{OV} can promote methane activation, while large ΔE_{*CH_3}

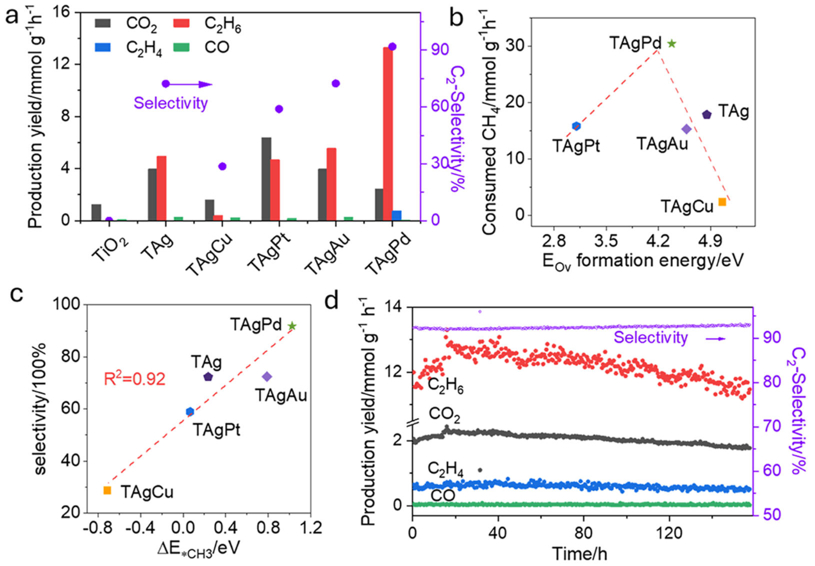

Figure 2. Experimental validation of activity-selectivity descriptors in POCM. (a) methane conversion rates and product distributions over a series of samples (including commercial TiO_2, TAg, TAgCu, TAgPt. TAgAu and TAgPd) under light irradiation. The bar graph shows product yields for CO_2 (black), C_2H_6 (red), C_2H_4 (blue), and CO (green), while the purple dots represent C_2 selectivity (C_2H_6 + C_2H_4); (b) relationship between methane consumption and the calculated O_v formation energy for different metal cocatalysts supported on anatase TiO_2, indicating that a proper O_v formation energy enhances methane activation; (c) selectivity toward C_2 products (C_2H_6 and C_2H_4) as a function of ΔE_{*CH_3}, showing that difference of CH_3 adsorption energies favor C−C coupling over overoxidation; (d) stability test of the TAgPd catalyst over continuous operation. Catalyst loading: 5 mg deposited on glass fiber filter paper. Reaction conditions: CH_4/O_2 (125/1 mL·min^{-1}) under illumination from a 300 W Xe lamp. The temporal evolution of CO_2, C_2H_6, C_2H_4, and CO production, and C_2 selectivity is plotted over time, demonstrating both high selectivity and good stability for C_2 product formation.

is beneficial for C_2 products generation. Among them, TAgPd exhibited the most favorable interfacial properties, achieving optimized E_{OV} and ΔE_{*CH_3} values that translated into a methane conversion rate exceeding 30 mmol g^{-1} h^{-1} with 92% selectivity toward C_2 hydrocarbons. Collectively, the long-standing activity-selectivity trade-off in POCM is quantitatively encoded by the $E_{OV}-\Delta E_{*CH_3}$ relationship and programmable through M−MO interaction. This will provide a generic design principle of catalysts by transforming phenomenological study to a testable, predictive, and quantitative approach.

■ RESULTS AND DISCUSSION

Theoretical Insights of Activity and Selectivity in POCM

In both C_2 and CO_2 generation pathways, the initial step involves cleavage of the first C−H bond in methane facilitated by lattice oxygen species of anatase, producing methyl radicals ($*CH_3$) and surface hydrogen (*H) as shown in Figure 1a. The removal of *H species consumes lattice oxygen, generating water and leaving an oxygen vacancy.[19] Thus, methane activation is intrinsically coupled to lattice oxygen consumption, making the E_{OV} a potential key parameter for evaluating methane conversion activity. Meanwhile, the $*CH_3$ will be either absorbed on the MO surface or migrate to metal surface. For those $*CH_3$ confined on the MO surface, are more likely to undergo further dehydrogenation and oxidation, eventually contributing to CO_2 formation. In contrast, the migration of $*CH_3$ to the metal cocatalyst surface increases the likelihood of C−C coupling for C_2 products. We note, however, that metal-bonded $*CH_3$ does not necessarily undergo coupling exclusively, as further dehydrogenation or other side reactions may also occur. Therefore, the key role of the cocatalyst is not to guarantee C_2 formation from every adsorbed $*CH_3$ species, but to provide a more coupling-favorable environment comparing to the oxidation-prone MO surface.[19] From this perspective, the selectivity toward C_2 products is expected to depend on the relative thermodynamic preference of methyl species for the metal surface ($E_{*CH_3\text{-M}}$) versus the MO surface ($E_{*CH_3\text{-MO}}$), which is quantified by the methyl adsorption energy difference (ΔE_{*CH_3}, $= E_{*CH_3\text{-M}} - E_{*CH_3\text{-MO}}$). Accordingly, ΔE_{*CH_3} should be viewed as a descriptor of methyl partitioning between coupling-favorable and oxidation-prone sites, rather than as a complete descriptor of all possible downstream reactions of $*CH_3$. Based on this understanding, we validate the proposed relationships through theoretical calculations and experimental verification.

To conduct the theoretical research, we build the different cocatalyst structures based on the anatase TiO_2, shown in Figure S1 (Supporting Information, SI). The interaction between supported metals and the TiO_2 lattice was found to significantly influence the O 2p band onset (the onset energy of the occupied O 2p states in the PDOS, referenced to the Fermi level), which in turn governs E_{OV}. Since the valence band maximum (VBM) of TiO_2 is dominated by O 2p states (Figure S2), an upward shift of the O 2p level can strengthen O 2p−Ti 3d antibonding hybridization, leading to weak Ti−O bonds with labile lattice oxygen for oxygen vacancy formation.[19] Calculations reveal that Ag-loaded TiO_2 exhibits an O 2p level at −2.69 eV, which is further shifted upward with Au (−2.62 eV), Pd (−2.50 eV), and Pt (−1.87 eV), or slightly downward with Cu (−2.81 eV). Such trend in O 2p level is consistent with their calculated E_{OV}. By correlating the O 2p energy level and E_{OV} (Figure 1b), a good linear relationship is found where higher O 2p level leads to lower E_{OV}. Based on this descriptor, TAgPt is predicted to deliver the highest lattice

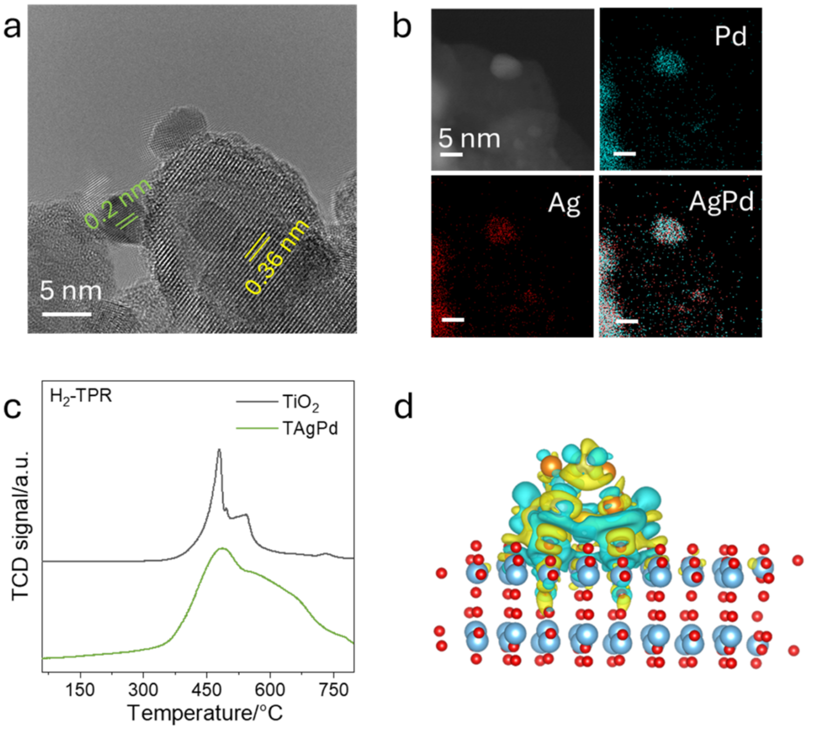

Figure 3. Structure of TAgPd and evidence of strong M−MO interaction. (a) High-resolution TEM (HRTEM) image illustrating clear lattice fringes of both AgPd particles and the anatase TiO_2 support, with measured interplanar spacings; (b) HAADF-STEM image and corresponding EDX elemental maps of Ag, Pd, and the Ag−Pd overlap, confirming homogeneous distribution at the nanoscale. The scale bar is 5 nm; (c) hydrogen temperature-programmed reduction (H_2-TPR) profiles collected under identical conditions for bare anatase (TiO_2, gray) and TAgPd (green): TAgPd displays an earlier leading edge and a broader main reduction band with a long tail, indicating reduced activation barriers and a wider distribution of sites for lattice-oxygen removal; (d) charge different analysis of TAgPd shows the charge transfer between metal and anatase, indicating electrons transfer from metal to anatase. The iso-surface value is 0.001 e Å^{-3}. Charge depletion and accumulation are labeled in cyan-color and yellow, respectively. Oxygen, titanium, sliver and palladium atoms are denoted as red, light blue, orange and dark blue balls, respectively.

oxygen activity and may show the highest performance in methane conversion. Additionally, the calculated E_{OV} values are site-dependent: oxygen atoms far from the M−MO interface behaves similarly to those in pristine TiO_2, while interfacial oxygen atoms are more easily removed. This result supports the viewpoint that the cocatalyst primarily perturbs and activates lattice oxygen in the interfacial region (Figure S3).

While E_{OV} is closely linked to methane activation and overall activity, product selectivity is dictated by the behavior of the $*CH_3$ intermediates. For example, as the predominant C_2 product, ethane (C_2H_6) is formed via coupling of two $*CH_3$ species, whereas CO_2 arises from their sequential oxidation (Figure 1a). The fate of $*CH_3$ depends on its preferential adsorption: migration to metal sites favors C−C coupling, whereas retention on oxide surfaces leads to overoxidation. To capture this effect, we computed the $*CH_3$ adsorption energy (E_{*CH_3}) on both TiO_2 ($E_{*CH_3\text{-}T}$) and the supported metal surfaces ($E_{*CH_3\text{-}M}$). As shown in Figure 1c, the binding strength on metal surfaces follows the order: TAgAu (−2.39 eV) > TAgPd (−2.13 eV) > TAg (−1.30 eV) > TAgPt (−1.09 eV) > TAgCu (−1.03 eV). In parallel, the adsorption strength on TiO_2 was also significantly modulated by the supported metals, confirming strong electronic coupling between the oxide and metal components, see the different $*CH_3$ adsorption structures in Figure S4. Generally, $*CH_3$ prefers the site with stronger adsorption. For most systems (TAg, TAgAu, TAgPd, TAgPt), $*CH_3$ adsorption is favored on the metal sites, while in TAgCu, $*CH_3$ binds more strongly to TiO_2. The proposed relative adsorption strength difference provides a rational descriptor for product selectivity. In systems where $*CH_3$ preferentially adsorbs on metal sites, C−C coupling is favored, enhancing C_2 selectivity. In contrast, when $*CH_3$ remains confined to TiO_2, deep oxidation dominates, lowering C_2 yields. Based on this descriptor, TAgPd is predicted to exhibit the highest selectivity toward C_2 products, whereas TAgCu is expected to show the lowest.

Experimental Validation of Structure-Performance Relationships

To experimentally establish the "structure−performance" relationships predicted by DFT, Ag-based metals were controllably loaded onto commercial TiO_2 (anatase) nanoparticles. Guided by theoretical insights, we synthesized a series of samples and evaluated their POCM performance in a continuous-flow reactor under Xe-lamp irradiation. As shown in Figure 2a, bare TiO_2 nanoparticles displayed negligible activity, yielding only CO_2 at a rate of 1.2 mmol g^{-1} h^{-1} without producing any C_2 products. In contrast, the introduction of Ag nanoparticles (TAg) significantly enhanced both activity and selectivity, achieving production rates of 6.46 mmol g^{-1} h^{-1} for C_2H_6 and 4.71 mmol g^{-1} h^{-1} for CO_2, corresponding to a C_2 selectivity of 72.3%. Incorporation of secondary metals further modulated performance. For example, Pt addition markedly promoted CO_2 formation, while Au favored higher C_2 yields. Most notably, TAgPd achieved outstanding performance, with production rates of

13.3 mmol g^{-1} h^{-1} (C_2H_6), 0.72 mmol g^{-1} h^{-1} (C_2H_4), 0.05 mmol g^{-1} h^{-1} (CO), and 2.43 mmol g^{-1} h^{-1} (CO_2), corresponding to a remarkable C_2 product selectivity of 92%. The different loading amounts were also scanned in Figure S5.

To connect these experimental findings with the above theoretical calculation results, methane consumption rates were plotted against the calculated E_{OV} values in Figure 2b. A volcano-type relationship was observed, with TAgPd at the peak. On the right side of the volcano, higher E_{OV} values reflect less reactive lattice oxygen and reduced methane activation. On the left side, however, excessively low E_{OV} values (e.g., in TAgPt) did not translate to higher activity. Instead, the overly active lattice oxygen promotes extended dehydrogenation, driving methane to complete oxidation into CO_2. Since the $CH_4 \rightarrow CO_2$ pathway consumes more oxygen per molecule than the $CH_4 \rightarrow C_2H_6$ route, such systems exhibit slower overall methane conversion. In contrast, TAgPd provides a balanced lattice oxygen activity that enables efficient C−H activation while suppressing deep oxidation, consistent with the optimal catalytic performance observed.

Selectivity trends were then correlated with the ΔE_{*CH_3} descriptor, defined as the adsorption energy difference of $*CH_3$ between TiO_2 and metal sites ΔE_{*CH_3} ($E_{*CH_3\text{-T}} - E_{*CH_3\text{-M}}$). As shown in Figure 2c, C_2 selectivity increased linearly with ΔE_{*CH_3}, highlighting that product distribution is governed by competitive CH_3 adsorption. Systems where $*CH_3$ preferentially binds to metal sites favor C−C coupling, while retention on the oxide surface leads to deep oxidation. TAgPd, with the largest ΔE_{*CH_3}, exhibited the highest C_2 selectivity, whereas TAgCu, with preferential adsorption on TiO_2, displayed the lowest. The synergy of moderately low E_{OV} and large ΔE_{*CH_3} renders TAgPd the most effective system, delivering the highest C_2H_6 production rate and selectivity among all samples.

The stability of TAgPd was further assessed under continuous-flow operation. As shown in Figure 2d, no significant deactivation was observed around 160 h of reaction, with C_2 product yields maintained around 14 mmol g^{-1} h^{-1} and selectivity consistently above 92%. The apparent quantum efficiency (AQE) for methane conversion reached 12.5% at 350 nm (Figure S6), placing TAgPd among the best-performing photocatalysts reported for POCM in terms of activity, selectivity, AQE, and long-term durability (Table S1 and Figure S7). Control experiments confirmed that the C_2 products originate exclusively from methane conversion (Figure S8). No detectable hydrocarbons were observed when methane was replaced with Ar, or when photocatalyst or light irradiation was omitted. Postreaction characterizations further confirmed the robustness of TAgPd: synchrotron powder diffraction (PD, Figure S9) and X-ray photoelectron spectroscopy (XPS, Figure S10) revealed no structural changes, while TEM imaging (Figure S11) showed stable AgPd particle sizes. Raman spectroscopy (Figure S12) detected no coke formation. Together, these results verify the high durability of TAgPd under continuous gas−solid POCM conditions.

Probing the Structure and M−MO Interaction of TAgPd

To further investigate the structure and interaction between metal and metal oxide, AgPd metal cocatalysts with tunable ratio of Ag and Pd were prepared. As shown in the Figure 3a, the as-synthesized metallic nanoparticles were loaded onto anatase with an average size of 4.5 nm (Figure S13) and displayed a lattice spacings of 0.20 nm attributed to (200) facet of Ag or Pd. Pristine commercial anatase TiO_2 nanoparticles shows a lattice spacing of ∼0.36 nm, corresponding to the anatase (101) plane in Figure S14. After metal loading, the morphology and lattice structure of the TiO_2 support remain essentially unchanged. In Figure S15, synchrotron-based powder diffraction (PD) patterns are collected with anatase TiO_2 (JCPDS #21−1272) as the main peak and some small peaks attributed to the metallic nanoparticles. According to the typical (111) diffraction peak of Ag and Pd, we have observed a shift of the (111) peak position with increasing Pd contents in Figure S16. Vegard's Law was applied to distinguish its structure from the single metal structure. As shown in Figure S17, it predicts a linear relationship between composition and lattice parameter, indicating the formation of a homogeneous solid solution. Furthermore, high-angle annular dark-field scanning transmission electron microscopy (HAADF-STEM) and corresponding energy dispersive X-ray (EDX) mapping were performed to further identify this nanostructure. The EDX mapping in Figure 3b reveals the homogeneous distribution of Ag and Pd, overlapping with the metallic crystal structure, confirming the mixture of the two metals, which further supports the PD analysis.

To reveal the interaction effect of cocatalysts on the anatase, hydrogen temperature-programmed reduction (H_2-TPR) was conducted, as shown in Figure 3c. Pristine anatase TiO_2 exhibits a narrow reduction peak centered at 480 °C with a shoulder peak at 540 °C, attributed to the removal of surface and subsurface lattice oxygen. By contrast, TAgPd shows an earlier onset and a broadened main band with a long, gradual tail rather than the sharp peak and steep decay of anatase. This downshifted leading edge and extended tail signify a continuum of lowered activation barriers for oxygen release, consistent with strong electronic coupling at the AgPd-TiO_2 interface that polarizes Ti−O bonds and facilitates vacancy formation and oxygen migration. Thus, the temperature distribution of the main peak and its tail demonstrates that lattice oxygen in TAgPd is intrinsically more labile and more reactive than in pristine anatase.

To probe the critical role of the M−MO interaction in governing interfacial charge redistribution, charge difference and Bader charge analysis were performed in Figure 3d. In the single-metal TAg system, Ag transfers a substantial 1.47 electrons directly to the oxide, reflecting a straightforward metal-to-oxide charge flow. In contrast, in the AgPd/TiO_2 system, the redistribution becomes more complex: Ag donates 0.91 electrons while Pd accepts a fraction 0.29 electrons, and the net charge transfer to TiO_2 is moderated (0.62 e^-). This indicates that the introduction of a second metal adds an additional degree of freedom, where charge can be partitioned both between the metal components and across the metal-oxide interface. The charge redistribution was verified by the high-resolution X-ray photoelectron spectroscopy (XPS). In Figure S18, it indicates the Ag 3d peaks shift from 367.5 eV for pure Ag, negatively to 366.6 eV for AgPd. The 1.1 eV negative shift suggests that incorporating Pd increases the electron density in the Ag d-band while decreasing the electron density in the sp-band.[8] This shift is consistent with previous reports.[8,29] To probe the local atomic environment, X-ray absorption spectroscopy (XAS) of Ag and Pd K edge were conducted (Figure S19), respectively. Distance of Pd−Pd (Figure S20) almost keeps no change, while Figure S21 and

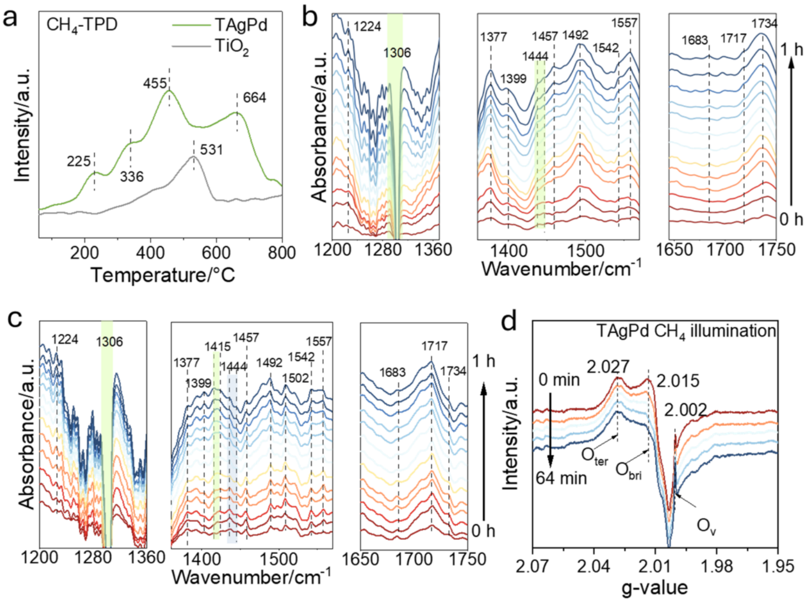

Figure 4. Mechanistic investigation of photocatalytic methane oxidation over various catalysts. (a) CH_4-TPD spectrum of TAgPd and pristine TiO_2; (b) in situ synchrotron-FTIR spectra under CH_4/O_2 (125/1 mL/min^{-1}) flow over TAgPd catalyst with light irradiation from 0 to 60 min (red to blue), revealing the formation and evolution of surface intermediates including CH_X, CH_3O^*, and $HCOO^*$; (c) in situ synchrotron-FTIR spectra under CH_4/O_2 (125/1 mL min^{-1}) over TAg catalyst; (d) Time-resolved in situ EPR spectra (0−64 min) tracking the dynamic evolution of the three species under photocatalytic methane activation.

Table S2 demonstrate that the distance of Ag−Ag decreased obviously compared to Ag foil, which is consistent with the observed lattice shrinkage.[8]

The above findings illustrate the crucial role of M−MO interactions in governing the performance. When metal nanoparticles are supported on the TiO_2 surface, strong interfacial coupling arises that alters the electronic structure of both components. On the one hand, the deposited metals can donate or withdraw charges from the TiO_2 lattice, thereby tuning the O 2p band onset and modulating the E_{OV}. This directly affects the availability and reactivity of lattice oxygen species for C−H bond activation. On the other hand, the presence of TiO_2 modifies the adsorption energetics of methyl intermediates on the metal sites, captured by the descriptor E_{*CH3}. The balance of these two effects: oxygen vacancy formation on the oxide and intermediate stabilization on the metal, ultimately determines whether methane is efficiently activated and whether $*CH_3$ couples selectively into C_2 products or undergoes overoxidation. Thus, the M−MO interaction serves as the fundamental origin of the dual-descriptor framework, linking atomic-scale interfacial phenomena to catalytic activity and selectivity.

Reaction Mechanisms investigations on TAgPd

To gain deeper insights into the POCM process on TAgPd, CH_4 temperature-programmed desorption (CH_4-TPD) was first conducted to evaluate methane adsorption on the catalyst surface. As shown in Figures 4a and S22, the introduction of metal significantly enhanced adsorption capacity, with desorption peaks shifting to lower temperatures and exhibiting larger areas compared to pristine TiO_2 (531 °C). Notably, TAgPd displayed four distinct desorption peaks at 225, 336, 455, and 664 °C, indicative of multiple adsorption sites and enhanced methane activation ability relative to bare TiO_2 and single-metal systems.

To investigate methane activation pathways, in situ synchrotron-based Fourier-transform infrared (FTIR) microspectroscopy was performed for TAgPd (Figure 4b) and TAg (Figure 4c). Negative peaks observed within 1261−1355 cm^{-1} spectral range with the main peak at 1306 cm^{-1} indicated methane consumption under illumination. The first C−H bond cleavage led to $*CH_3$ formation, observed at 1399 and 1492 cm^{-1} on both TAg and TAgPd.[30,31] Subsequent oxidation yielded $*OCH_3$ intermediates (1436, 1444 cm^{-1}), precursors to CO_2.[17,32] Notably, TAg exhibited much stronger $*OCH_3$ signals, suggesting their accumulation on Ag and their tendency to undergo further oxidation, consistent with higher CO_2 selectivity. Indeed, downstream oxidation products including HCHO (1717, 1734 cm^{-1}), $HCOO^-$ (1415, 1423, 1542, 1557 cm^{-1}), HCO_3^- (1683 cm^{-1}), and $*CO_3^{2-}$ (1224, 1397, 1502 cm^{-1}) were observed predominantly on TAg,[17,20,31,33] highlighting extensive overoxidation. By contrast, these intermediates appeared with much lower intensities on TAgPd, demonstrating that Pd incorporation suppresses overoxidation. Instead, new peaks at 1377 and 1457 cm^{-1}, attributable to $*CH_2CH_3$ species, were detected on TAgPd but negligible on TAg, suggesting that Pd facilitates the C−C coupling and subsequent dehydrogenation of ethane to ethylene.[17] Compared with the metal-loaded samples, bare TiO_2 exhibits only very weak surface intermediate signals, indicating its limited ability to activate CH_4 and generate detectable reaction intermediates under photocatalytic conditions (Figure S23).

To probe reactive surface species under working conditions, in situ electron paramagnetic resonance (EPR) spectroscopy was employed. Under N_2, TAgPd exhibited an intrinsic oxygen vacancy signal at g = 2.00249, which intensified under illumination (Figure S24), confirming light-induced vacancy formation.[34] Upon O_2 exposure, the signal intensity decreased, consistent with vacancy refilling. In contrast, pure anatase (Figure S25) showed signals at g = 1.985 (Ti^{3+}), indicating

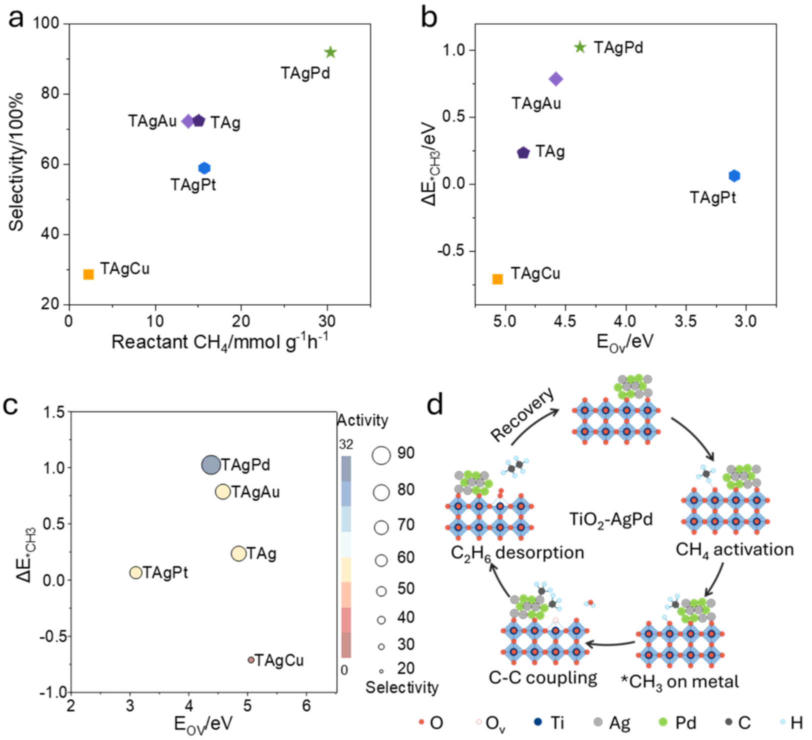

Figure 5. Correlation between catalyst descriptors, methane conversion, and product selectivity. (a) Relationship between methane conversion rate and C_2 (C_2H_4 + C_2H_6) selectivity, showing a positive correlation where enhanced methane activation favors C−C coupling. (b) Two-dimensional volcano-like trend between oxygen vacancy formation energy (E_{OV}) and methyl adsorption energy difference (ΔE_{*CH_3}), highlighting the synergistic influence of lattice oxygen reactivity and methyl adsorption energetics on catalytic performance. The deviation observed for TAgPt indicates that excessively low E_{OV} may lead to overoxidation, reducing C_2 selectivity despite high methane conversion. (c) Two-dimensional descriptor map correlating catalytic performance with oxygen-vacancy formation energy (E_{OV}) and methyl adsorption-energy difference (ΔE_{*CH_3}). The symbol color denotes catalytic activity (consumed methane/mmol g^{-1} h^{-1}), and the symbol size represents selectivity (C_2 products/%). The distribution of the data points highlights the coupled influence of lattice-oxygen reactivity and methyl adsorption energetics on overall performance. (d) Schematic illustration of the proposed photocatalytic reaction loop on AgPd/TiO_2.

photogenerated electrons trapped by Ti^{4+}.[34] The absence of Ti^{3+} signals in TAgPd suggests that electrons are effectively extracted from TiO_2 by the alloy nanoparticles, preventing bulk charge trapping. When methane was introduced, new oxygen-related species were observed (Figure 4d). Signals at $g = 2.015$, 2.011, and 2.001 were assigned to bridging $O^{\bullet-}$ (O_{bri}) species, while those at $g = 2.027$, 2.013, and 2.004 correspond to terminal $O^{\bullet-}$ (O_{ter}) species formed via hole trapping at lattice oxygen sites.[15,34] The progressive increase of the $g = 2.002$ signal indicated the creation of oxygen vacancies during methane activation. Importantly, the O_{ter} signal remained stable throughout the 0−64 min illumination period, suggesting hole accumulation in lattice oxygen. The simultaneous buildup of O_{bri} and only limited vacancy formation indicates that lattice oxygen extraction is kinetically difficult, making vacancy formation a likely rate-determining step, consistent with prior reports.[19] Upon introduction of mixed CH_4/O_2 feeds (Figure S26), both O_{ter} and O_{bri} signals diminished, confirming their active participation in the catalytic cycle. In the absence of gaseous O_2, that is, under a pure CH_4 feed, TAgPd exhibits a pronounced decline in catalytic performance relative to that observed under mixed CH_4/O_2 conditions (Figure S27). Only very limited product formation is observed, indicating that O_2 plays a crucial role in sustaining methane conversion in this system. This result suggests that O_2 is not merely a background component but is essential for maintaining the active oxygen species and enabling efficient catalytic turnover. Therefore, O_2 is a key participant in the reaction network and is indispensable for achieving high activity under the present POCM conditions.

Based on the combined in situ EPR and synchrotron-FTIR results, lattice oxygen activation and vacancy formation are central to methane activation, but the selectivity of subsequent steps depends critically on how $*CH_3$ intermediates are stabilized at the M−MO interface. In TAgPd, efficient electron extraction prevents Ti^{3+} accumulation, balanced lattice oxygen activity enables controlled C−H activation, and the interfacial environment suppresses OCH_3 overoxidation while promoting C−C coupling pathways. This mechanistic evidence provides direct spectroscopic validation of the DFT-predicted descriptors (E_{OV} and ΔE_{*CH_3}), establishing a coherent picture of why TAgPd achieves both high activity and selectivity in POCM.

Materials Design Principles

To elucidate the combined effects of E_{OV} and ΔE_{*CH_3} on methane activation and C_2 product formation, we carried out a two-dimensional correlation analysis (Figure 5). As shown in Figure 5a, methane conversion rate and C_2 selectivity are positively correlated: catalysts that activate methane more efficiently also favor multicarbon products over undesired byproducts. This observation underscores that efficient methane activation intrinsically facilitates C−C coupling. The mechanistic origin of this trend can be traced to the dual descriptors. Methane conversion is primarily governed by the reactivity of lattice oxygen, reflected in E_{OV}. Lower

E_{OV} values correspond to more labile oxygen reservoirs, enabling facile C−H bond cleavage and higher conversion rates. In contrast, C_2 selectivity is dictated by ΔE_{*CH_3}, which determines the relative adsorption preference of methyl intermediates between oxide and metal sites, thereby controlling whether $*CH_3$ radicals undergo coupling or deep oxidation. The interplay of these two factors is further illustrated in Figure 5b, which reveals a volcano-type dependence of performance, which shows the similar relationship in Figure 2b. On the ascending branch, moderately low E_{OV} values promote methane activation, while larger ΔE_{*CH_3} differences favor selective CH_3 coupling, delivering both high conversion and selectivity. However, when E_{OV} becomes excessively low, oxygen species become overly reactive, driving CH_3 toward full oxidation into CO_x rather than C−C coupling. For example, TAgPt lies on this descending side of the volcano, where ultralow E_{OV} suppresses C_2 selectivity despite facile C−H activation. By contrast, TAgPd resides in the optimal window, achieving a balance between lattice oxygen reactivity and methyl adsorption energetics that maximizes both methane conversion and C_2 selectivity. These findings establish a general design principle for POCM: co-optimization of lattice oxygen activity (E_{OV}) and methyl adsorption balance (ΔE_{*CH_3}) is essential to achieve high performance. More broadly, this dual-descriptor framework provides predictive guidance for the design of advanced photocatalysts in selective oxidation and C−C coupling reactions, where strong bond activation must be delicately balanced against the suppression of overoxidation pathways. To deepen our understanding, the two-dimensional map was shown in Figure 5c. It correlates catalytic performance with E_{OV} and ΔE_{*CH_3}. Here, the symbol color represents activity, and the symbol size reflects selectivity. The map shows that high activity is associated with a relatively large ΔE_{*CH_3}, whereas high selectivity appears in the region combining a large E_{OV} with a small ΔE_{*CH_3}. Among the examined samples, TAgPd is in the high-activity and the highest selectivity region. Figure 5d summarizes the proposed photocatalytic reaction loop on AgPd/TiO_2. Under illumination, methane is activated at the metal−semiconductor interface to form surface methyl species, accompanied by H transfer and the involvement of lattice oxygen from TiO_2. The generated methyl intermediates subsequently undergo coupling to produce C_2 hydrocarbons, while the oxide surface is regenerated through the interfacial redox cycle. This scheme highlights the cooperative roles of the AgPd bimetallic sites and the TiO_2 support, in which the metal component promotes methane activation and intermediate coupling, whereas the oxide lattice participates in oxygen transfer and catalyst turnover.

To examine the generality of this framework, AgPd was further supported on different oxide hosts, including Anatase-O_V, ZnO, CeO_2, and commercial TiO_2 (P25). As shown in Figure S28, these systems exhibited markedly different activities and C_2 selectivity, indicating that M−MO interactions modulate both the metal and oxide components and thereby reshape the overall catalytic behavior. Accordingly, the correlation among E_{OV}, ΔE_{*CH_3} and catalytic performance is not universal in a single quantitative sense but depends on the specific interfacial interaction. This generality is not limited to oxide variation alone: the cocatalyst identity is also an integral part of the M−MO interaction, and different metals are likewise expected to alter electronic coupling, oxygen reactivity, and methyl-site preference, leading to distinct yet related E_{OV}, ΔE_{*CH_3} landscapes. Thus, while the dual-descriptor framework captures the essential trade-off governing POCM, each metal/oxide family may define its own descriptor map. This result highlights an important direction for the field: developing catalyst-family specific descriptor landscapes that integrate both metal and oxide contributions, enabling a more predictive design strategy for selective methane conversion.

■ CONCLUSION

Through a combined theoretical-experimental investigation, we established a dual-descriptor framework that rationalizes and predicts activity and selectivity of POCM. Density functional theory calculations identified two interfacial parameters E_{OV} and ΔE_{*CH_3} as decisive factors controlling activity and selectivity. E_{OV} reflects the availability and reactivity of lattice oxygen, with moderately low values promoting efficient C−H activation, whereas excessively low values drive CH_3 overoxidation into CO_x. In parallel, ΔE_{*CH_3} governs the stabilization and fate of CH_3 intermediates, where balanced adsorption energetics enable migration to metal sites and selective C−C coupling into C_2 hydrocarbons, while unbalanced adsorption favors complete oxidation. Ag-based systems supported on TiO_2 validate this framework: AgPd achieves the optimal balance of descriptors, delivering a C_2 yield of 14 mmol g^{-1} h^{-1} with 92% selectivity, an AQE of 12.5% at 350 nm, and stability around 160 h. In situ EPR and synchrotron-FTIR results further confirm that vacancy dynamics and moderated CH_3 stabilization at the metal−oxide interface underpin the superior selectivity of AgPd. Extending this analysis to different oxide supports reveals that each host defines its own E_{OV}−ΔE_{*CH_3} landscape, highlighting the support-dependent nature of descriptor−performance relationships. Collectively, these results demonstrate that E_{OV} and ΔE_{*CH_3} enable a quantitative description of M−MO interactions by linking interfacial electronic structure to catalytic function, thereby providing a generalizable design principle for selective methane conversion and a predictive framework for understanding metal−metal oxide interfaces.

■ ASSOCIATED CONTENT

Supporting Information

The Supporting Information is available free of charge at https://pubs.acs.org/doi/10.1021/jacs.6c01783.

Detailed experimental procedures, catalyst synthesis details, material characterization (PD, XPS, TEM, XAS, FTIR, EPR, CH_4-TPD), photocatalytic performance measurements, DFT computational results (PDF)

■ AUTHOR INFORMATION

Corresponding Authors

Zhiliang Wang − *Nanomaterials Centre, School of Chemical Engineering and Australian Institute for Bioengineering and Nanotechnology, The University of Queensland, St Lucia, QLD 4072, Australia;* orcid.org/0000-0003-2139-8495; Email: zhiliang.wang@uq.edu.au

Lianzhou Wang − *Nanomaterials Centre, School of Chemical Engineering and Australian Institute for Bioengineering and Nanotechnology, The University of Queensland, St Lucia, QLD 4072, Australia; Department of Applied Biology and Chemical Technology, The Hong Kong Polytechnic University, Kowloon 999077 Hong Kong SAR, China;* Email: lianzhou.wang@polyu.edu.hk

Authors

Yanzhao Zhang − *Nanomaterials Centre, School of Chemical Engineering and Australian Institute for Bioengineering and Nanotechnology, The University of Queensland, St Lucia, QLD 4072, Australia;* orcid.org/0000-0003-2894-4727

Jiakang You − *Nanomaterials Centre, School of Chemical Engineering and Australian Institute for Bioengineering and Nanotechnology, The University of Queensland, St Lucia, QLD 4072, Australia*

Kai Wang − *Nanomaterials Centre, School of Chemical Engineering and Australian Institute for Bioengineering and Nanotechnology, The University of Queensland, St Lucia, QLD 4072, Australia; Department of Applied Biology and Chemical Technology, The Hong Kong Polytechnic University, Kowloon 999077 Hong Kong SAR, China*

Dazhi Yao − *Commonwealth Scientific and Industrial Research Organization (CSIRO) Mineral Resources, Pullenvale, QLD 4069, Australia;* orcid.org/0000-0002-8019-0160

Haijiao Lu − *Nanomaterials Centre, School of Chemical Engineering and Australian Institute for Bioengineering and Nanotechnology, The University of Queensland, St Lucia, QLD 4072, Australia;* orcid.org/0000-0001-9273-2898

Jitraporn Vongsvivut − *Infrared Microspectroscopy (IRM) Beamline, ANSTO-Australian Synchrotron, Clayton, VIC 3168, Australia;* orcid.org/0000-0003-0699-3464

Jingwei Hou − *Nanomaterials Centre, School of Chemical Engineering and Australian Institute for Bioengineering and Nanotechnology, The University of Queensland, St Lucia, QLD 4072, Australia;* orcid.org/0000-0001-9139-9835

Peng Chen − *Nanomaterials Centre, School of Chemical Engineering and Australian Institute for Bioengineering and Nanotechnology, The University of Queensland, St Lucia, QLD 4072, Australia;* orcid.org/0000-0001-8634-4717

Yonggang Jin − *Commonwealth Scientific and Industrial Research Organization (CSIRO) Mineral Resources, Pullenvale, QLD 4069, Australia*

Gang Liu − *Shenyang National Laboratory for Materials Science, Institute of Metal Research, Chinese Academy of Sciences, Shenyan 110016, China; School of Materials Science and Engineering, University of Science and Technology of China, Shenyang 110016, China;* orcid.org/0000-0002-6946-7552

Complete contact information is available at: https://pubs.acs.org/10.1021/jacs.6c01783

Notes

The authors declare no competing financial interest.

■ ACKNOWLEDGMENTS

Z.W. and L.W. acknowledge the support of the Australian Research Council through its Future Fellowship (FT230100251), DECRA (DE210100930), Discovery (DP200101900) and Laureate Fellowship (FL190100139) schemes. G.L. acknowledges the support by the National Natural Science Foundation of China (Nos. 52120105003, 52425201). The authors acknowledge the facilities, and the scientific and technical assistance, of the Australian Microscopy and Microanalysis Research Facility at the Centre for Microscopy and Microanalysis, The University of Queensland. This research was undertaken on the PD, XAS and IRM beamlines at the Australian Synchrotron, part of ANSTO. This research was undertaken with the assistance of resources from the National Computational Infrastructure (NCI Australia), an NCRIS enabled capability supported by the Australian Government. This work was supported by resources provided by the Pawsey Supercomputing Research Centre's Setonix Supercomputer (10.48569/18sb-8s43), with funding from the Australian Government and the Government of Western Australia. L.W. acknowledges the financial support from HKSAR Global STEM Professorship, and the JC STEM Lab of Renewable Energy Materials funded by The Hong Kong Jockey Club Charities Trust.

■ REFERENCES

(1) Li, X.; Li, C.; Xu, Y.; Liu, Q.; Bahri, M.; Zhang, L.; Browning, N. D.; Cowan, A. J.; Tang, J. Efficient hole abstraction for highly selective oxidative coupling of methane by Au-sputtered TiO_2 photocatalysts. *Nat. Energy* **2023**, *8* (9), 1013−1022.

(2) Wang, H.; Qi, H.; Sun, X.; Jia, S.; Li, X.; Miao, T. J.; Xiong, L.; Wang, S.; Zhang, X.; Liu, X.; et al. High quantum efficiency of hydrogen production from methanol aqueous solution with PtCu−TiO_2 photocatalysts. *Nat. Mater.* **2023**, *22* (5), 619−626.

(3) Yu, X.; Zholobenko, V. L.; Moldovan, S.; Hu, D.; Wu, D.; Ordomsky, V. V.; Khodakov, A. Y. Stoichiometric methane conversion to ethane using photochemical looping at ambient temperature. *Nat. Energy* **2020**, *5* (7), 511−519.

(4) Xia, B.; Zhang, Y.; Ran, J.; Jaroniec, M.; Qiao, S.-Z. Single-Atom Photocatalysts for Emerging Reactions. *ACS Cent. Sci.* **2021**, *7* (1), 39−54.

(5) Wang, H.; Lee, H.-W.; Deng, Y.; Lu, Z.; Hsu, P.-C.; Liu, Y.; Lin, D.; Cui, Y. Bifunctional non-noble metal oxide nanoparticle electrocatalysts through lithium-induced conversion for overall water splitting. *Nat. Commun.* **2015**, *6* (1), No. 7261.

(6) Park, S. H.; Kim, S.; Park, J. W.; Kim, S.; Cha, W.; Lee, J. In-situ and wavelength-dependent photocatalytic strain evolution of a single Au nanoparticle on a TiO_2 film. *Nat. Commun.* **2024**, *15* (1), No. 5416.

(7) Clavero, C. Plasmon-induced hot-electron generation at nanoparticle/metal-oxide interfaces for photovoltaic and photocatalytic devices. *Nat. Photonics* **2014**, *8* (2), 95−103.

(8) Zamora Zeledón, J. A.; Stevens, M. B.; Gunasooriya, G. T. K. K.; Gallo, A.; Landers, A. T.; Kreider, M. E.; Hahn, C.; Nørskov, J. K.; Jaramillo, T. F. Tuning the electronic structure of Ag-Pd alloys to enhance performance for alkaline oxygen reduction. *Nat. Commun.* **2021**, *12* (1), No. 620.

(9) Song, S.; Song, H.; Li, L.; Wang, S.; Chu, W.; Peng, K.; Meng, X.; Wang, Q.; Deng, B.; Liu, Q.; et al. A selective Au-ZnO/TiO_2 hybrid photocatalyst for oxidative coupling of methane to ethane with dioxygen. *Nat. Catal.* **2021**, *4* (12), 1032−1042.

(10) Jiang, W.; Low, J.; Mao, K.; Duan, D.; Chen, S.; Liu, W.; Pao, C.-W.; Ma, J.; Sang, S.; Shu, C.; et al. Pd-modified ZnO−Au enabling alkoxy intermediates formation and dehydrogenation for photocatalytic conversion of methane to ethylene. *J. Am. Chem. Soc.* **2021**, *143* (1), 269−278.

(11) Chen, Y.; Zhao, Y.; Liu, D.; Wang, G.; Jiang, W.; Liu, S.; Zhang, W.; Li, Y.; Ma, Z.; Shao, T.; et al. Continuous flow system for highly efficient and durable photocatalytic oxidative coupling of methane. *J. Am. Chem. Soc.* **2024**, *146* (4), 2465−2473.

(12) Wang, C.; Xu, Y.; Xiong, L.; Li, X.; Chen, E.; Miao, T. J.; Zhang, T.; Lan, Y.; Tang, J. Selective oxidation of methane to C_{2+}

products over Au-CeO_2 by photon-phonon co-driven catalysis. *Nat. Commun.* **2024**, *15* (1), No. 7535.

(13) Ma, J.; Tan, X.; Zhang, Q.; Wang, Y.; Zhang, J.; Wang, L. Exploring the size effect of Pt nanoparticles on the photocatalytic nonoxidative coupling of methane. *ACS Catal.* **2021**, *11* (6), 3352−3360.

(14) Zhang, Y.; Xia, B.; Ran, J.; Davey, K.; Qiao, S. Z. Atomic-Level reactive sites for semiconductor-based photocatalytic CO_2 reduction. *Adv. Energy Mater.* **2020**, *10* (9), No. 1903879.

(15) Li, X.; Wang, C.; Yang, J.; Xu, Y.; Yang, Y.; Yu, J.; Delgado, J. J.; Martsinovich, N.; Sun, X.; Zheng, X.-S.; et al. PdCu nanoalloy decorated photocatalysts for efficient and selective oxidative coupling of methane in flow reactors. *Nat. Commun.* **2023**, *14* (1), No. 6343.

(16) Chen, Z.; Wu, S.; Ma, J.; Mine, S.; Toyao, T.; Matsuoka, M.; Wang, L.; Zhang, J. Non-oxidative coupling of methane: N-type doping of Niobium single atoms in TiO_2−SiO_2 induces electron localization. *Angew. Chem., Int. Ed.* **2021**, *60* (21), 11901−11909.

(17) Lyu, Y.; Xu, R.; Williams, O.; Wang, Z.; Sievers, C. Reaction paths of methane activation and oxidation of surface intermediates over NiO on Ceria-Zirconia catalysts studied by In-situ FTIR spectroscopy. *J. Catal.* **2021**, *404*, 334−347.

(18) Chai, Y.; Tang, S.; Wang, Q.; Wu, Q.; Li, L.; Liang, J. Nickel phosphide nanoparticles as a noble-metal-free co-catalyst for the selective photocatalytic aerobic oxidation of CH_4 into CO and H_2. *J. Catal.* **2023**, *425*, 306−313.

(19) Zhai, G.; Cai, L.; Ma, J.; Chen, Y.; Liu, Z.; Si, S.; Duan, D.; Sang, S.; Li, J.; Wang, X.; et al. Highly efficient, selective, and stable photocatalytic methane coupling to ethane enabled by lattice oxygen looping. *Sci. Adv.* **2024**, *10* (26), No. eado4390.

(20) Chen, X.; Li, Y.; Pan, X.; Cortie, D.; Huang, X.; Yi, Z. Photocatalytic oxidation of methane over silver decorated zinc oxide nanocatalysts. *Nat. Commun.* **2016**, *7* (1), No. 12273.

(21) Wang, P.; Shi, R.; Zhao, Y.; Li, Z.; Zhao, J.; Zhao, J.; Waterhouse, G. I. N.; Wu, L.-Z.; Zhang, T. Selective photocatalytic oxidative coupling of methane via regulating methyl intermediates over Metal/ZnO Nanoparticles. *Angew. Chem., Int. Ed.* **2023**, *62* (23), No. e202304301.

(22) You, J.; Bao, Y.; Zhang, Y.; Konarova, M.; Wang, Z.; Wang, L. Green energy driven methane conversion under mild conditions. *EES Catal.* **2024**, *2* (6), 1210−1227.

(23) Wang, Y.; Hong, G.; Zhang, Y.; Liu, Y.; Cen, W.; Wang, L.; Wu, Z. Photocatalytic oxidative coupling of methane over Au_1Ag single-atom alloy Modified ZnO with oxygen and water vapor: Synergy of gold and silver. *Angew. Chem., Int. Ed.* **2023**, *62* (42), No. e202310525.

(24) Hu, C.; Mu, X.; Fan, J.; Ma, H.; Zhao, X.; Chen, G.; Zhou, Z.; Zheng, N. Interfacial effects in PdAg bimetallic nanosheets for selective dehydrogenation of formic acid. *ChemNanoMat* **2016**, *2* (1), 28−32.

(25) Wang, L.; Jin, J.; Li, W.; Li, C.; Zhu, L.; Zhou, Z.; Zhang, L.; Zhang, X.; Yuan, L. Highly selective catalytic oxidation of methane to methanol using Cu−Pd/anatase. *Energy Environ. Sci.* **2024**, *17*, 9122−9133.

(26) Tan, Z.; Li, X.; Bai, R.; Guo, C.; Han, X.; Shi, J.; Zhang, J.; Li, H. AI for complex catalytic systems: high-entropy alloys in electrocatalytic acetylene semihydrogenation. *ACS Catal.* **2025**, *15* (15), 13097−13106.

(27) He, T.; Sun, R.; Shi, R.; Chen, X.; Zhou, T.; Han, Y.; Liu, F.; Cui, H.; Li, H.; Liu, Q. From dopant periodicity to asymmetric sites: steering C−C coupling in single-atom alloy catalysts for electrochemical CO_2 reduction. *Angew. Chem., Int. Ed.* **2026**, *65*, No. e20426.

(28) You, J.; Zhang, Y.; Wang, Z.; Yin, H.; Zhao, G.; Steele, J.; Vongsvivut, J.; Riches, J.; Wang, K.; Yao, D.; Lu, H.; Bao, Y.; Peng, X.; Chen, P.; Chen, P.; Du, A.; Jin, Y.; Wang, L. Tuning reaction pathway with surface metal cocatalyst for ethylene production via photocatalytic methane conversion. *J. Am. Chem. Soc.* **2025**, *147* (47), 44011−44020.

(29) Coulthard, I.; Sham, T. K. Charge redistribution in Pd-Ag alloys from a local perspective. *Phys. Rev. Lett.* **1996**, *77* (23), 4824−4827.

(30) Zhang, Y.; Johannessen, B.; Zhang, P.; Gong, J.; Ran, J.; Qiao, S.-Z. Reversed electron transfer in dual single atom catalyst for boosted photoreduction of CO_2. *Adv. Mater.* **2023**, *35* (44), No. 2306923.

(31) Feng, N.; Lin, H.; Song, H.; Yang, L.; Tang, D.; Deng, F.; Ye, J. Efficient and selective photocatalytic CH_4 conversion to CH_3OH with O_2 by controlling overoxidation on TiO_2. *Nat. Commun.* **2021**, *12* (1), No. 4652.

(32) He, Y.; Guo, F.; Yang, K. R.; Heinlein, J. A.; Bamonte, S. M.; Fee, J. J.; Hu, S.; Suib, S. L.; Haller, G. L.; Batista, V. S.; Pfefferle, L. D. *In situ* identification of reaction intermediates and mechanistic understandings of methane oxidation over hematite: A combined experimental and theoretical study. *J. Am. Chem. Soc.* **2020**, *142* (40), 17119−17130.

(33) Ftouni, K.; Lakiss, L.; Thomas, S.; Daturi, M.; Fernandez, C.; Bazin, P.; El Fallah, J.; El-Roz, M. TiO_2/Zeolite bifunctional (photo)catalysts for a selective conversion of methanol to dimethoxymethane: On the role of brønsted acidity. *J. Phys. Chem. C* **2018**, *122* (51), 29359−29367.

(34) Kumar, C. P.; Gopal, N. O.; Wang, T. C.; Wong, M.-S.; Ke, S. C. EPR Investigation of TiO_2 nanoparticles with temperature-dependent properties. *J. Phys. Chem. B* **2006**, *110* (11), 5223−5229.